Supporting Information

Zou et al. 10.1073/pnas.1420785112

SI Materials and Methods

Cell Lines, Culture, Viability, and Kinase Assays. HCC78 human NSCLC cells and BaF3 cells were obtained from DSMZ and NIH-3T3 cells were purchased from American Tissue Culture Corporation. Cells were maintained using standard culture techniques. All engineered cell lines were generated with the pMSCV retroviral system (Clontech). Cell-based kinase phosphorylation assays were performed in 0.5% serum. Compounds were added to the cells for 1 h and lysates were used to determine the levels of phospho-ROS1 and total ROS1 using PathScan Sandwich ELISA Kit (Cell Signaling, catalog nos. 7093 and 7091, respectively) as described in the manufacturer's protocol. The IC_{50} values were calculated by concentration-response curve fitting utilizing a four-parameter analytical method. Cell growth was assayed by seeding cells in growth media containing 10% (vol/vol) FBS and culturing in serial dilutions of compounds for 72 h. A Cell Titer Glo assay (Promega) was then performed to determine the relative cell numbers. IC_{50} values were calculated by concentration-response curve fitting utilizing a four-parameter analytical method.

Statistical Analysis. Data were analyzed using a two-tailed *t* test or ANOVA. Due to skewed distribution of the tumor volume data, ANOVA models were fit to the rank-transformed data. Individual comparisons between treatment groups and vehicle group or among the treatment groups were assessed with one-sided least significant difference tests, and all were assessed under the ANOVA model for ranks.

Expression and Purification of Human ROS1 Kinase Domain. The sequence (MAHHHHHHDYGIPTTENLYFQGS) encoding 6XHis and a tobacco etch virus (TEV) protease cleavage site was fused to the N terminus of the human ROS1 kinase domain (residues 1934–2232) using PCR amplification and then was cloned into the pFastBac1 insect cell expression vector (Life Technologies). A baculovirus stock was generated, Sf21 cells were infected, and cells were harvested 72 h after infection. Frozen cell pellets were lysed in the lysis buffer [50 mM Tris (pH 8.0), 150 mM NaCl, 10% glycerol, and one Roche Complete Protease Inhibitor Mixture Tablet (Roche Applied Science) per 50 mL of lysis buffer] with 1.5 mL of buffer/1g of cell pellet. Immobilized metal affinity chromatography (IMAC) purification was performed using a ProBond nickel-chelating resin (Life Technologies) according to the manufacturer's protocol. The protein then was dephosphorylated with purified histidine-tagged Lambda phosphatase, and the histidine tag was cleaved by digestion at 4 °C overnight with TEV protease in lysis buffer supplemented with 20 mM imidazole. The digested protein was loaded back onto an IMAC column, and flow through containing the cleaved ROS1 kinase domain was collected, concentrated, and loaded on Superdex 75 16/60 column pre-equilibrated with 25 mM Hepes (pH 7.4), 150 mM NaCl, 5% glycerol, and 2 mM Tris(2-carboxyethyl)phosphine (TCEP). Monomer peaks containing the ROS1 kinase were pooled together and subjected to in vitro autophosphorylation at room temperature in 25 mM Hepes (pH 7.4), 150 mM NaCl, 5% glycerol, 2 mM TCEP, 20 mM MgCl2, and 5 mM ATP. The autophosphorylation reaction was stopped with EDTA pH 8.0 (final concentration 100 mM) when the protein reached a +3P, +4P state, as monitored by LCMS. EDTA was removed using a Superdex 75 16/60 column, and fractions containing predominantly +3P protein were collected and concentrated to 12.2 mg/mL for crystallization.

ROS1 Biochemical Kinase Assays. Biochemical inhibition of wild-type and mutant ROS1 kinase activity was determined using a microfluidic mobility shift assay as previously described (1). Reactions containing 0.9 nM wild-type ROS1, 2.5 nM $ROS1^{G2032R}$, and 2.3 nM $ROS1^{L2026M}$ were initiated with ATP (7.8–1,000 μM) and allowed to proceed for 1 h at room temperature. K_i values were determined from global fits of the initial rates to a tight-binding equation for competitive inhibition (1) using nonlinear regression (GraphPad Prism; GraphPad Software) after the inhibitors were shown to be competitive with ATP. Before use, enzymes were activated by autophosphorylation by incubating 30 μM proteins with 4 mM Mg ATP and confirming the 3P-phospho state by LC-MS.

Generation of the Engineered ROS1 Cell Line. Selected human ROS1 fusion genes first were cloned into the retroviral vector pMSCV puro or pMSCVhygro. The retroviruses carrying recombinant genes were produced in 293T cells by cotransfection with the pMSCV vectors and the packaging plasmid pCL10A1. The retroviral supernatants were used to transduce NCI-H3122, NIH 3T3, or BaF3 parental cells, and pooled populations were selected with 2 g/mL puromycin or 50 g/mL hygromycin for 5 d.

Cellular ROS1 Phosphorylation ELISA Assay. Cells were seeded in 96-well plates in growth medium with 0.5% serum and incubated overnight. Compounds were diluted in medium without serum, added to the cells, incubated for 1 h, and then removed by aspirating the medium by vacuum suction. Cell lysates were generated, and the phospho-ROS1 (Tyr2274) levels were determined by using the PathScan Phospho-ROS1 (panTyr) Sandwich ELISA Kit (catalog no. 7093; Cell Signaling) as described in the manufacturer's protocol. The IC_{50} values were calculated by concentration–response curve fitting using a four-parameter analytical method.

Cell Proliferation Assay. Cells were seeded in 96-well plates in growth medium containing 10% FBS and were cultured overnight at 37 °C. The following day, serial dilutions of PF-06463922 or appropriate controls were added to the designated wells, and cells were incubated at 37 °C for 72 h. A CellTiter-Glo assay (Promega) was performed to determine the relative cell numbers. IC_{50} values were calculated by concentration–response curve fitting using a four-parameter analytical method.

Crystal Structure. Crystals were obtained by the hanging-drop vapor-diffusion method at 13 °C by mixing 1.5 μL of solution containing a 1:3 molar ratio of phosphorylated ROS1 kinase domain (12.2 mg/mL) to PF-06463922 and 1.5 μL of reservoir solution containing 25% (wt/vol) PEG 3350, 0.6 M potassium thiocyanate, and 0.1 M sodium citrate tribasic dihydrate (pH 5.6). Crystals were flash-frozen in liquid nitrogen after transfer to a 2-μL reservoir solution containing 25% (vol/vol) glycerol as a cryoprotectant. An X-ray dataset (Rmerge = 0.038 for data in the range of 92–2.21 Å) was collected at beamline 17-ID at the Advanced Photon Source synchrotron (Argonne National Laboratories). The structure was solved with the CNX 2005 (2) and Coot (3) program packages using the previously determined ROS1–crizotinib complex structure (PDB ID code 3ZBF) as the starting model. The refined ROS1 PF-06463922 structure has an R-factor of 0.212 and an R-free of 0.280 for data to 2.4 Å.

s.c. Tumor Growth Inhibition Studies. Female nu/nu mice were obtained from Charles River Laboratories. Animals were maintained under clean-room conditions in sterile filter-top cages with

ALPHA-Dri bedding (Shepherd) and were housed on HEPA-filtered ventilated racks. Animals received sterile rodent chow and water ad libitum. The cultured cells were harvested in serum-free medium and were supplemented with 50% Matrigel (BD Biosciences) to facilitate tumor take. Cells (5×10^6 in 100 μL) were implanted s.c. into the hind flank region of the mouse and allowed to grow to the designated size before the administration of compound for each experiment. The compound of interest was administered either orally at 5–10 mL/kg using the sterile 20-G feeding needles (Popper and Sons, Inc., or via an s.c. Alzet minipump (DURECT Corporation) infusion. Tumor size was determined by measurement with an electronic caliper, and tumor volume was calculated as the product of length × width^2 × 0.4.

FIG-ROS1 GBM Model. De novo GBM tumorigenesis was initiated in LSL-FIG-ROS1;Cdkn2a$^{-/-}$;LSL-Luc mice through intracranial stereotactic injections of Adeno-Cre as described previously (4). Tumor development was monitored using BLI as described below. Once tumors reached a given size ($>10^7$ p^{-1}·s^{-1}·cm^{-2}·sr^{-1}), animals were randomly enrolled into vehicle control or 3-, 7-, or 14-d treatment with the indicated doses of PF-06463922. Drug was administered through s.c. implanted Alzet osmotic pumps. After treatment, mice were killed, GBM tumors were microdissected, and tissues were flash-frozen in liquid N_2. The remaining brains were processed for histology. Protein lysates were derived using snap-frozen tumor tissues, and FIG-ROS1 proteins were immunoprecipitated. The immunoprecipitated materials then were subjected to Western blotting against ROS1 using a phospho-specific antibody (pY2274) to determine the levels of autophosphorylated FIG-ROS1, which are a direct measure of FIG-ROS1 kinase activity.

Immunoblotting. The immunoblotting method also was used to determine relative kinase phosphorylation status and total protein levels of the protein of interest in cells and tumor tissues. Protein samples extracted from cells or tumor lysates were separated by SDS/PAGE and transferred to nylon membranes, and immunoblotting hybridizations for the proteins of the interest were performed using the corresponding antibodies.

IHC Staining. Following standard tissue collection, xenograft tumor specimens were formalin-fixed, paraffin-embedded, and sectioned at a thickness of 4–5 μm onto positively charged microscope slides. Deparaffinization, rehydration, antigen retrieval, and IHC staining techniques were performed using the fully automated BOND MAX instrument or BOND-III Staining System instrument (Leica Microsystems). Heat-induced epitope retrieval was performed with Leica Bond Epitope Retrieval Solution 1 or 2. Nonspecific immunolabeling was reduced with Cyto Q Background Buster (Innovex Biosciences) or Protein Block from either Dako or Spring Bioscience. The specific primary antibody was detected using the Leica Bond Polymer Refine Detection system. Before immunolabeling development with 3,3′diaminobenzidine tetrahydrochloride, endogenous peroxidase activity was blocked with hydrogen peroxide. All tumor sections were counterstained with hematoxylin, dehydrated, cleared, and mounted before histological evaluation.

Tumor Histology and IHC Scoring. IHC scoring was conducted by the board-certified pathologists. Positive and negative control slides for each marker were evaluated to ensure the specificity of the staining. All samples were evaluated for cellular staining patterns (compared with controls) to ensure that consistent staining was present and to establish the range of the staining frequency, distribution, and intensity. Any discrepancies noted in staining consistency prompt additional or repeat staining before evaluation. Once the consistency of staining was confirmed, the staining frequency/distribution and staining intensity (if notably variable between samples) were tabulated for all samples; one or more additional slide reviews were done at the conclusion of the initial evaluation to confirm patterns observed on the initial evaluation. Mean values and the range of staining scores were evaluated between groups, and notable differences and/or patterns were compared between samples from vehicle (or untreated) and treated animals and between individual treatment groups.

1. Williams JW, Morrison JF (1979) The kinetics of reversible tight-binding inhibition. *Methods Enzymol* 63:437–467.
2. Brünger AT, et al. (1998) Crystallography & NMR system: A new software suite for macromolecular structure determination. *Acta Crystallogr D Biol Crystallogr* 54(Pt 5): 905–921.
3. Emsley P, Lohkamp B, Scott WG, Cowtan K (2010) Features and development of Coot. *Acta Crystallogr D Biol Crystallogr* 66(Pt 4):486–501.
4. Charest A, et al. (2006) ROS fusion tyrosine kinase activates a SH2 domain-containing phosphatase-2/phosphatidylinositol 3-kinase/mammalian target of rapamycin signaling axis to form glioblastoma in mice. *Cancer Res* 66(15):7473–7481.

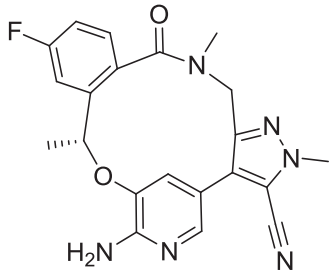

Fig. S1. Chemical structure of PF-06463922, (10R)-7-Amino-12-fluoro-2,10,16-trimethyl-15-oxo-10,15,16,17-tetrahydro-2H-8,4-(metheno)pyrazolo[4,3-h][2,5,11]-benzoxadiazacyclotetradecine-3-carbonitrile.

Kinase[a]	Enzyme Selectivity	
	Enzyme IC50 (Ki[b]) (nM)	Selectivity ratio
ROS1	<0.025[b]	1
ALK	<0.07[b]	≥2.8
ALK^{L1196M}	0.7[b]	>28
LTK	2.7	>108
FER	3.3	>132
FES (FPS)	6	>240
PTK2B (FAK2)	14	>560
TNK2 (ACK)	17	>680
PTK2 (FAK)	17	>680
TRKB	23	>920
TRKA	24	>960
TRKC	46	>1000
FRK (PTK5)	53	>1000
EGFR$^{L858R/T790M}$	56	>1000
EGFR^{T790M}	319	>1000
JAK2	529	>1000

on-target Activity

100% of 206 Invitrogen kinases showed selectivity ratios >100-fold vs. ROS1

[a:] Top "hits" in Invitrogen 206 kinases panel (>75% inhibition at 1uM).

[b:] bInhibition constants (Ki) from in-house microfluidic mobility-shift assays.

Fig. S2. PF-06463922 kinase selectivity relative to ROS1.

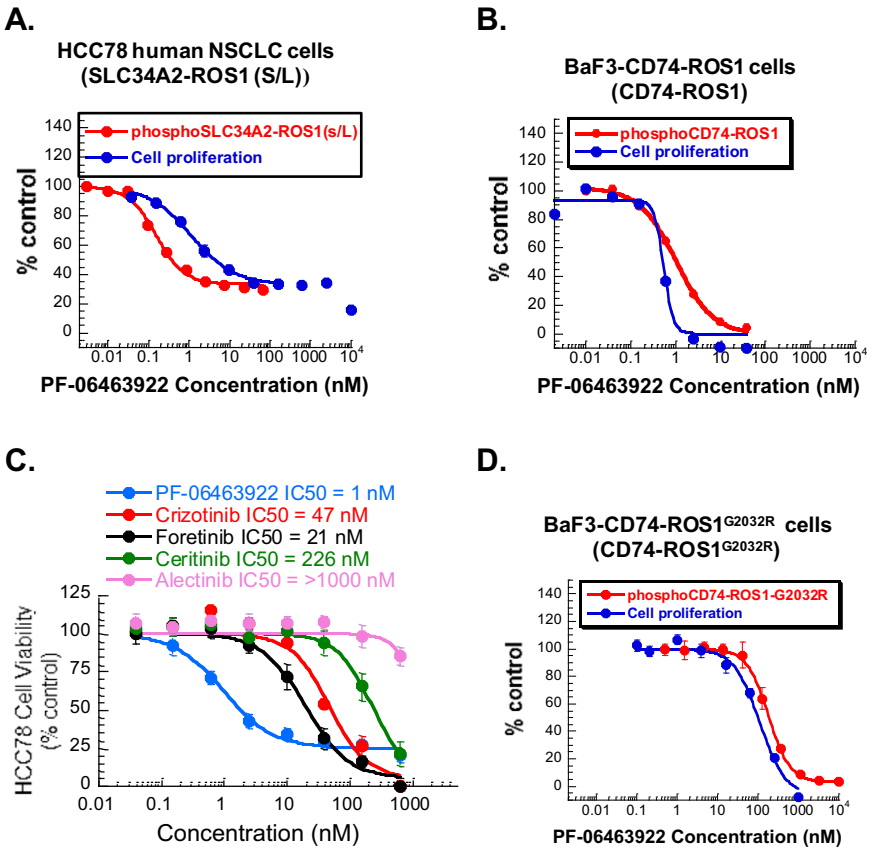

Fig. S3. PF-06463022 inhibited the ROS1 autophosphorylation and cell proliferation in the HCC78, BaF3-CD74-ROS1 cells expressing ROS1 fusion variants containing wild-type ROS1 (*A* and *B*). Comparison of antiproliferative effect of PF-06463922 to crizotinib, ceritinib, alectinib, and foretinib in the HCC78 cell viability assays (representative dose–response curves) (*C*). PF-06463922 inhibited ROS1 phosphorylation and cell proliferation in the BaF3-CD74-ROS1^{G2032R} cells expressing CD74-ROS1^{G2032R} fusion (*D*). The values are shown as mean + SD; $n = 3$.

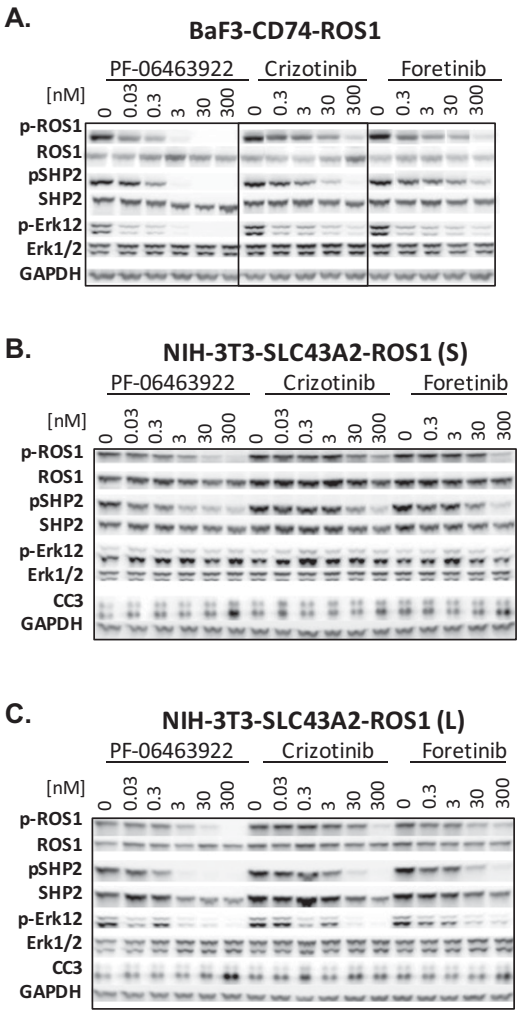

Fig. S4. Comparison of PF-06463922, crizotinib, and foretinib on ROS1 fusion-mediated signal transduction in Ba/F3 cells expressing human CD74-ROS1 (*A*) and in NIH 3T3 cells expressing human SLC34A2-ROS1 (S) (*B*) and SLC34A2-ROS1 (L) (*C*).

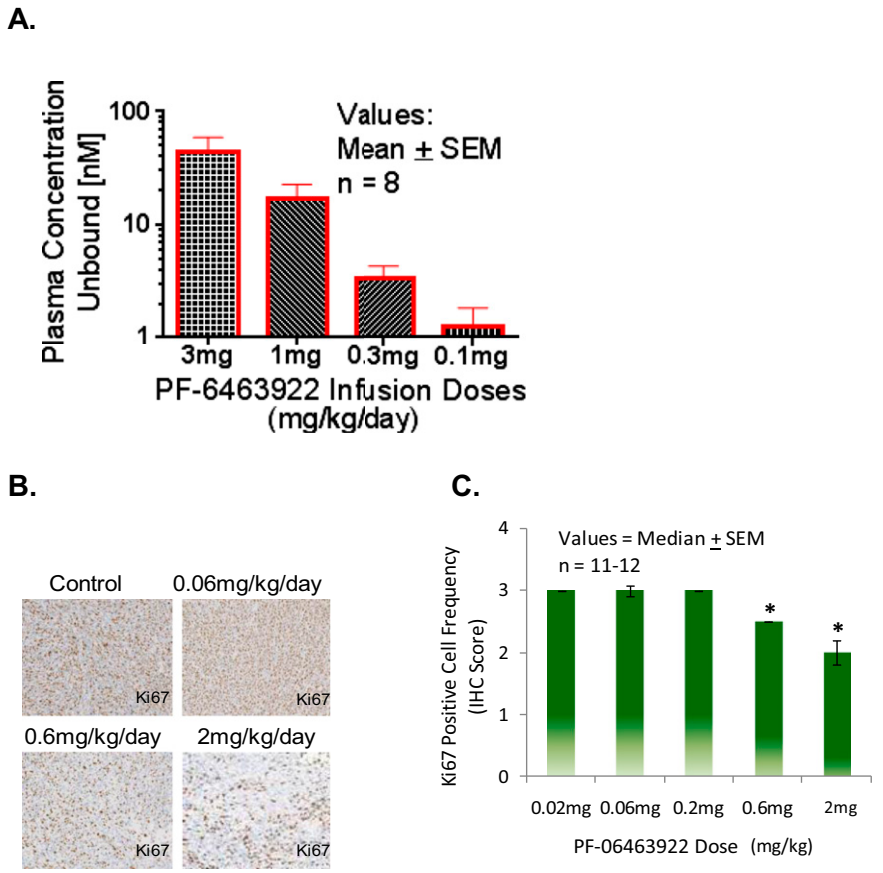

Fig. S5. (*A*) Unbound plasma concentrations of PF-06463922 following 7 d of pump infusion in mice bearing NIH 3T3-FIG-ROS1(S) tumors. (*B* and *C*) PF-06463922 dose-dependently reduced the number of Ki67-positive cells in the NIH 3T3-CD74-ROS1 tumors. (*B*) Representative images of Ki67-stained s.c. tumor sections from the NIH 3T3-CD74-ROS1 tumors following 9 d of treatment with vehicle or indicated dose levels of PF-06463922. (*C*) Bar graph showing the median IHC scores of Ki67-positive cell numbers in the NIH 3T3-CD74-ROS1 tumors. *$P < 0.0001$ by one-way ANOVA.

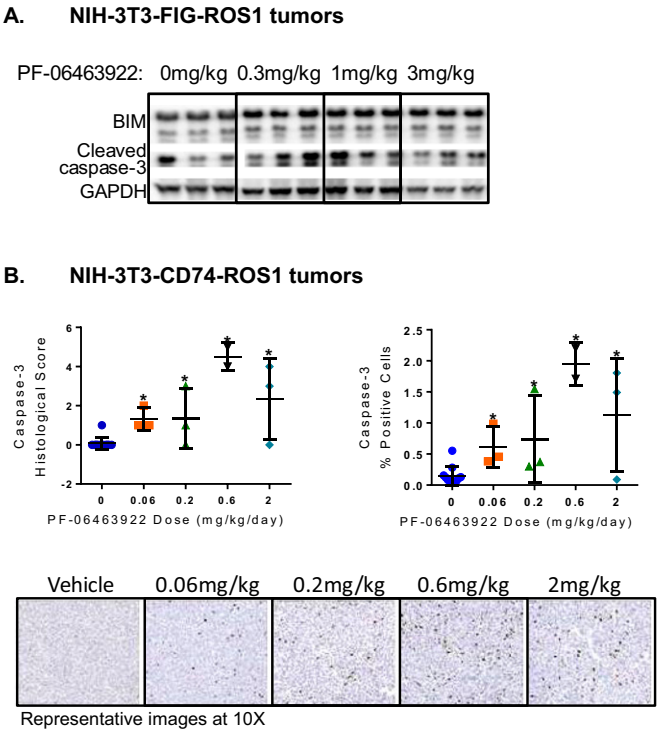

Fig. S6. Cleaved caspase 3 or BIM levels following PF-06463922 treatment in the xenograft tumors expressing FIG-ROS1 (*A*), CD74-ROS1 (*B*), and CD74-ROS1^{G2032R} (*C*). *$P \leq 0.015$ determined by one-way ANOVA.

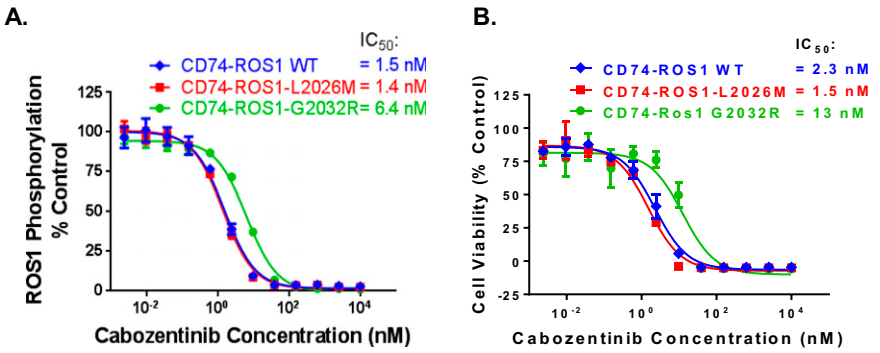

Fig. S7. Cabozantinib potencies against ROS1 kinase activity (*A*) and cell proliferation (*B*) in the engineered BaF3 cells expressing CD74-ROS1, CD74-ROS1^{L2026M}, and CD74-ROS1^{G2032R}.

Table S1. ROS1 fusion genes in cancer

5′ fusion	Chromosome	Type	Clinical	Frequency, %	References
FIG	6q22.1	Deletion	Glioblastoma	—	(1–3)
			NSCLC	2	(4, 5)
			Cholangiocarcinoma	9	(6)
			Ovarian cancer		(7)
CD74	5q32	Interchromosomal	NSCLC		(4, 8–12)
SLC34A2	4p15.2	Interchromosomal	NSCLC		(4, 8–12)
			Gastric cancer		(13)
			Colorectal cancer		(14)
TPM3	1q21.2	Interchromosomal	NSCLC		(12)
			Spitzoid neoplasm		(15)
SDC4	20q12	Interchromosomal	NSCLC		(12)
EZR	6q25.3	Paracentric inversion	NSCLC		(12)
LRIG3	12q14.1	Interchromosomal	NSCLC		(12)
KDELR2	7p22.1	Interchromosomal	NSCLC		(8)
CCDC6	10q21	Interchromosomal	NSCLC		(11)
CEP85L	6q22.31	Deletion	Angiosarcoma	3	(16)
			Glioblastoma		(17)
YWHAE (14-3-3 ε)	17p13.3	Interchromosomal	Infl. myofibroblastic	3.5	(18, 19)
TFG	3q12.2	Interchromosomal	Infl. myofibroblastic	3.5	(18, 19)
HLA-A	6p21.3	Intrachromosomal	Spitzoid neoplasm		(15)
MYO5A	15q21	Interchromosomal	Spitzoid neoplasm		(15)
PPFIBP1	12p12.1	Interchromosomal	Spitzoid neoplasm		(15)
ERC1	12p13.3	Interchromosomal	Spitzoid neoplasm		(15)
PWWP2A	5q33.3	Interchromosomal	Spitzoid neoplasm		(15)
CLIP1	12q24.3	Interchromosomal	Spitzoid neoplasm		(15)
ZCCHC8	12q24.3	Interchromosomal	Spitzoid neoplasm		(15)
KIAA1598	10q25.3	Interchromosomal	Spitzoid neoplasm		(15)

1. Birchmeier C, O'Neill K, Riggs M, Wigler M (1990) Characterization of ROS1 cDNA from a human glioblastoma cell line. *Proc Natl Acad Sci USA* 87(12):4799–4803.
2. Charest A, et al. (2003) Oncogenic targeting of an activated tyrosine kinase to the Golgi apparatus in a glioblastoma. *Proc Natl Acad Sci USA* 100(3):916–921.
3. Charest A, et al. (2003) Fusion of FIG to the receptor tyrosine kinase ROS in a glioblastoma with an interstitial del(6)(q21q21). *Genes Chromosomes Cancer* 37(1):58–71.
4. Rimkunas VM, et al. (2012) Analysis of receptor tyrosine kinase ROS1-positive tumors in non-small cell lung cancer: Identification of a FIG-ROS1 fusion. *Clin Cancer Res* 18(16):4449–4457.
5. Suehara Y, et al. (2012) Identification of KIF5B-RET and GOPC-ROS1 fusions in lung adenocarcinomas through a comprehensive mRNA-based screen for tyrosine kinase fusions. *Clin Cancer Res* 18(24):6599–6608.
6. Gu TL, et al. (2011) Survey of tyrosine kinase signaling reveals ROS kinase fusions in human cholangiocarcinoma. *PLoS ONE* 6(1):e15640.
7. Birch AH, et al. (2011) Chromosome 3 anomalies investigated by genome wide SNP analysis of benign, low malignant potential and low grade ovarian serous tumours. *PLoS ONE* 6(12):e28250.
8. Govindan R, et al. (2012) Genomic landscape of non-small cell lung cancer in smokers and never-smokers. *Cell* 150(6):1121–1134.
9. Rikova K, et al. (2007) Global survey of phosphotyrosine signaling identifies oncogenic kinases in lung cancer. *Cell* 131(6):1190–1203.
10. Rimkunas V, et al. (2010) Frequencies of ALK and ROS in NSCLC FFPE tumor samples utilizing a highly specific and sensitive immunohistochemistry-based assay and FISH analysis. *J Clin Oncol* 28(Suppl 15):10536 (abstr).
11. Seo JS, et al. (2012) The transcriptional landscape and mutational profile of lung adenocarcinoma. *Genome Res* 22(11):2109–2119.
12. Takeuchi K, et al. (2012) RET, ROS1 and ALK fusions in lung cancer. *Nat Med* 18(3):378–381.
13. Lee J, et al. (2013) Identification of ROS1 rearrangement in gastric adenocarcinoma. *Cancer* 119(9):1627–1635.
14. Aisner DL, et al. (2014) ROS1 and ALK fusions in colorectal cancer, with evidence of intratumoral heterogeneity for molecular drivers. *Mol Cancer Res* 12(1):111–118.
15. Wiesner T, et al. (2014) Kinase fusions are frequent in Spitz tumours and spitzoid melanomas. *Nat Commun* 5:3116.
16. Giacomini CP, et al. (2013) Breakpoint analysis of transcriptional and genomic profiles uncovers novel gene fusions spanning multiple human cancer types. *PLoS Genet* 9(4):e1003464.
17. Stransky N, Cerami E, Schalm S, Kim JL, Lengauer C (2014) The landscape of kinase fusions in cancer. *Nat Commun* 5:4846.
18. Lovly CM, et al. (2014) Inflammatory myofibroblastic tumors harbor multiple potentially actionable kinase fusions. *Cancer Discov* 4(8):889–895.
19. Lovly CM, et al. (2013) Potentially actionable kinase fusions in inflammatory myofibroblastic tumors. *J Clin Oncol* 31(Suppl):10513 (abstr).

Table S2. PF-06463922 IC_{50} values in cells harboring ROS1 fusion variants

Target	PF-06463922	Crizotinib	Foretinib	Ceritinib	Alectinib	Assays
HCC78 (endogenous)						
SLC34A2-ROS1	0.19 ± 0.14	51 ± 23	99 ± 17	>1,000	>1,000	Cellular pROS1 IC_{50} (nM)
	1.15 ± 0.48	21 ± 4.4	19 ± 3.3	506 ± 203	>10,000	Cell proliferation IC_{50} (nM)
BaF3 (engineered)						
CD74-ROS1	0.23 ± 0.22	3.9 ± 0.92	3.8 ± 2.12	71 ± 53	>10,000	Cellular pROS1 IC_{50} (nM)
CD74-ROS1^{G2032R}	203 ± 46	>5,000	88 ± 59	>2,000	>10,000	Cellular pROS1 IC_{50} (nM)
CD74-ROS1^{L2026M}	0.57 ± 0.13	230 ± 11	9.9 ± 3.7	70 ± 27	>10,000	Cellular pROS1 IC_{50} (nM)
CD74-ROS1	0.62 ± 0.64	18 ± 23	11 ± 4.2	44 ± 37.4	>2,000	Cell proliferation IC_{50} (nM)
CD74-ROS1^{G2032R}	177 ± 128	>2,000	69 ± 11	>2,000	>2,000	Cell proliferation IC_{50} (nM)
CD74-ROS1^{L2026M}	1.1 ± 0.13	259 ± 11	8.6 ± 1.5	60 ± 11	>2,000	Cell proliferation IC_{50} (nM)
NIH 3T3 (engineered)						
CD74-ROS1	0.53 ± 0.21	11+3.6	5.47 ± 2.6	341 ± 102	>5,000	Cellular pROS1 IC_{50} (nM)
FIG-ROS1(S)	0.24 ± 0.12	60+37	6.1 ± 1.9	488 ± 180	>5,000	Cellular pROS1 IC_{50} (nM)
FIG-ROS1(L)	0.20 ± 0.10	41+27	5.6 ± 4.9	304 ± 85	>5,000	Cellular pROS1 IC_{50} (nM)

n = 1–8.

Table S3. Biochemical potency (K_i) of ALK inhibitors for wild-type and mutant ROS1

K_i*	ROS1, nM	ROS1^{L2026M}, nM	ROS1^{G2032R}, nM
PF-06463922	<0.025	0.10 ± 0.01	12.0 ± 0.5
Crizotinib	0.6 ± 0.2	5.8 ± 0.2	330 ± 10
Foretinib	8.2 ± 0.4	16 ± 1	20 ± 1
Ceritinib	0.7 ± 0.1	0.4 ± 0.1	230 ± 10
Alectinib†	2,400 ± 100	2,000 ± 100	>3,000

*K_i values were determined by inhibitor titration at multiple ATP concentrations and fitting data (n = 2) to a tight binding equation for competitive inhibition, as described in *SI Materials and Methods* and shown in Fig. S2. Values represent globally fit K_i values ± SE of the fit. $K_{M,ATP}^{app}$ was determined at nonsaturating phosphoacceptor substrate concentrations to be 65 μM, 147 μM, and 22 μM for ROS1, ROS1^{L2026M}, and ROS1^{G2032R}, respectively.
†Projected K_is from partial dose–response curves because this compound seemed to have solubility/aggregation issues at >3 μM.

Dataset S1. Dose-dependent inhibition of PF-06463922, crizotinib, foretinib, ceritinib, and alectinib against recombinant wild-type and mutant ROS1 kinase in biochemical assays

Dataset S1

ATP was varied from 7.8 to 1,000 μM as shown. Fractional inhibition velocities (vi/vo) were measured using a microfluidic mobility-shift assay and were globally fit to a tight-binding equation for competitive inhibition to calculate K_i constants (summarized in Table S3) as described in *SI Materials and Methods*. Alectinib failed to inhibit ROS1G2032R under the dose ranges tested.

Dataset S2. Mode of inhibition for PF-06463922, crizotinib, foretinib, ceritinib, and alectinib against recombinant wild-type and mutant ROS1 kinase in biochemical assays

Dataset S2

Tight-binding IC_{50} values (Kiapp) displayed a linear dependence on ATP concentration, consistent with ATP competitive inhibition. Inhibition data were determined using a mobility-shift assay as described in *SI Materials and Methods*.